https://doi.org/10.1016/j.ijmecsci.2020.105509

Advancing Elastic Wave Imaging Using Thermal Susceptibility of Acoustic Nonlinearity

Kai Wang [a], Wuxiong Cao [a], Menglong Liu [b], Yehai Li [c,d], Pengyu Zhou [a], Zhongqing Su [a,*]

[a] Department of Mechanical Engineering
The Hong Kong Polytechnic University, Kowloon, Hong Kong SAR

[b] School of Mechanical Engineering and Automation, Harbin Institute of Technology, Shenzhen 518052, P.R. China

[c] Guangdong Provincial Key Lab of Robotics and Intelligent System
Shenzhen Institutes of Advanced Technology, Chinese Academy of Sciences, Shenzhen 518052, P.R. China

[d] CAS Key Laboratory of Human-Machine Intelligence-Synergy Systems
Shenzhen Institutes of Advanced Technology, Shenzhen 518052, P.R. China

submitted to ***International Journal of Mechanical Sciences***
(Initial submission on 7 November 2019; first revision and re-submission on 29 December 2019; second revision and re-submission on 17 January 2020; third revision and re-submission on 28 January 2020)

* To whom correspondence should be addressed. Tel.: +852-2766-7818, Fax: +852-2365-4703;

Email: Zhongqing.Su@polyu.edu.hk (Prof. Zhongqing SU, *Ph.D.*)

Abstract

Despite proven effectiveness in characterizing material degradation and embryonic defects, the use of acoustic nonlinearity is restricted by its intrinsic vulnerability to measurement contamination and to fluctuations in ambient temperature in particular. Analytically, we shed light on the susceptibility of acoustic nonlinearity embodied in elastic waves to ambient temperature. Rather than eliminating or compensating for such thermal susceptibility, we subtly exploit it to advance nonlinear elastic wave imaging. Experimental validation corroborates theoretical prediction, spotlighting the capacity of the approach to improve the precision of material characterization using nonlinear elastic waves and therefore to enhance the accuracy of anomaly imaging when other nonlinearity sources interfere with the extraction of nonlinear attributes of elastic waves.

Keywords: elastic wave propagation; acoustic nonlinearity; elastic wave imaging; thermal susceptibility; material characterization

1. Introduction

Acoustic nonlinearity embodied in elastic waves features greater sensitivity than its linear counterparts to subtle changes in material properties, even when the changes are minimal. This characteristic provides a physical cornerstone on which basis diverse material characterization techniques have been deployed, as typified by microstructure inspection [1-3], defect evaluation [4-6], tissue pathology [7, 8], and therapeutic applications [9, 10]. Central to the interest is leveraging acoustic nonlinearity to non-destructively gauge material degradation (*e.g.*, dislocation, vacancy, grain boundary, micro-crack) induced by various causes including manufacturing glitches, in-service loads, ageing or environmental attacks [4, 11, 12].

The effectiveness of using acoustic nonlinearity for material characterizing lies in the premise that the material anomalies can introduce or augment the material acoustic nonlinearity, and consequently modulate the probing elastic waves and generate nonlinear attributes in elastic waves, as typified by the second harmonic generation of elastic waves. Representatively, Deng [13] and De Lima et al. [14], respectively, investigated the generation of second harmonic wave modes in plate-like waveguides analytically, linking the second harmonic generation with the acoustic nonlinearity parameter. Cantrell et al. [15] proposed a model to interpret the effect of dislocation dipoles on the material acoustic nonlinearity and presented experimental evidence. Xiang et al. [16] developed an analytical model to describe the influence of mixed dislocations on acoustic nonlinearity in plastically deformed materials. Kim et al. [17] and Sohn et al.[18], respectively, tracked the change of acoustic nonlinearity parameter and nonlinear wave modulation with the evolution of fatigue damage using experimental approaches. These researches have unveiled the effect of material anomalies on the acoustic nonlinearity and demonstrated the superb potentials of using nonlinear wave features for material characterization.

Despite considerable previous investigations of the physical nature of acoustic nonlinearity, precise acquisition of the nonlinear attributes of elastic waves remains a daunting task in measurement practice, precluding the use of delicate nonlinear attributes of elastic waves for calibrating material acoustic nonlinearity – a challenge attributable to the extremely low magnitude of material acoustic nonlinearity, that results in the marked susceptibility of nonlinear wave features to other sources of nonlinearity than the material nonlinearity itself. These sources include environmental contamination (e.g., temperature fluctuation), and testing apparatus among others[19].

Continued efforts [20-22] have been made to isolate these non-material-related acoustic nonlinearity sources and consequently minimize their contribution to the overall nonlinearity of elastic wave signals in measurement, thereby enhancing the precision of material characterization and anomaly imaging. Nevertheless, it is envisaged that these undesirable nonlinearity sources can only be more or less reduced rather than entirely eliminated. Prevailing endeavors do not provide a generic solution for effective elimination of the adverse effects of numerous sources of nonlinearity on wave feature extraction. Among various non-material-related sources of acoustic nonlinearity, the thermal variation is usually a concern which can alter propagation attributes of waves [22-26]. To put it into perspective, a variation of 0.1°C in temperature can lead to a shift of 0.01% in the resonant frequency, which is comparable with the intrinsic material nonlinearity, as reported elsewhere [25]. Together with other nonlinearity sources, these practical factors can remarkably contaminate the measurement of nonlinear features of elastic waves. These contaminations suffice to erode the confidence in material characterization or anomaly imaging using the acoustic nonlinearity extracted from elastic wave signals. In contrast, exploitation of the benign aspects of the thermal susceptibility of nonlinear attributes of elastic waves, rather than eliminating or compensating for its adverse effect, has ushered in a new avenue to enhance the accuracy, precision and reliability of the use of acoustic nonlinearity. This approach entails rigorous interpretation of the thermal attributes of nonlinear wave features. Taking advantage of those thermal attributes, the material phase change (from a cubic structure to a tetragonal structure) of a selected waveguide ($SrTiO_3$) is evaluated experimentally [27], and the interfacial stress between matrix and reinforcements in composites is quantified [28, 29].

Considering that the material anomaly can alter the thermal susceptibility of wave nonlinearity to a salient degree, we exploit such a phenomenon to improve material characterization and anomaly imaging using acoustic nonlinearity. With this motivation, we achieve an analytical insight into the thermal susceptibility of a particular nonlinear attribute of elastic waves (i.e., the second harmonic generation) to variation of ambient temperature, and on this basis the effect of material anomaly on thermal susceptibility is investigated, to advance nonlinear elastic wave-based anomaly imaging. Accurately extracted and quantified material acoustic nonlinearity gives anomaly imaging enhanced precision and accuracy, and this allows experimental validation to be followed, in which a fatigue crack can be imaged with higher precision, compared with conventional acoustic nonlinearity-based methods. This approach is physically underpinned by the fact that the extent of thermal susceptibility of nonlinear attributes of elastic waves manifests differently in accordance with the different physical properties of materials. The merits of this study mainly include the interpretation of the effect of material anomaly on the thermal susceptibility of nonlinear wave features, and also the use of this defect-altered thermal susceptibility to enhance the precision and accuracy of material characterization and anomaly imaging using the acoustic nonlinearity.

2. Theoretical principle: thermal susceptibility of nonlinear attributes of elastic waves

The intrinsic acoustic nonlinearity of a material can be depicted analytically using the material's nonlinear elastic moduli – a physical property commonly referred to as the *third-order-elastic tensor*. Macroscopically, such nonlinearity mirrors the shift of acoustic energy from the incident frequency band to other frequencies; microscopically, it is in essence linked to the interatomic bonding in the material, namely the interatomic force and interatomic distance. Atomic bonding is governed by the interatomic potential that calibrates the potential energy of a system of atoms and the material deformation at the atomic scale. There is no lack of physical models that are capable of approximating the interatomic potential between neutral atoms [30-33], such as the embedded atom model, the Lennard-Jones potential, the Sutton-Chen potential, and the glue potential, to name a few. In particular, the Lennard-Jones potential reads

$$E_{L\text{-}J}(r) = 4w\left[\left(\frac{q_{L\text{-}J}}{r}\right)^{12} - \left(\frac{q_{L\text{-}J}}{r}\right)^{6}\right], \tag{1}$$

where $E_{L\text{-}J}(r)$ signifies the interatomic potential – a function of the interatomic distance r. w and $q_{L\text{-}J}$ denote two empirical parameters accounting for the depth of the potential well and the distance between two atoms at which the potential is zero, respectively. **Fig. 1** depicts the correlation between $E_{L\text{-}J}(r)$ and r.

As temperature increases, the kinetic energy of atoms in the material rises correspondingly, augmenting the magnitude of atomic vibration and interatomic potential. Because the Lennard-Jones potential is "an-harmonic", the average interatomic separation increases, as shown in **Fig. 1**. Here, the interatomic separation is defined, at a given potential, using the mean value of the interatomic distances of the repulsive branch and the attractive branch. This consequently leads to macroscopic thermal expansion of the material.

By virtue of the linearized thermal expansion theory [34], the interatomic distance r can be correlated to temperature T as

$$r\left(T\right)=r_0[1+\alpha\left(T-T_0\right)], \tag{2}$$

where α is the thermal expansion coefficient of the material; $T-T_0$ is the temperature change from the reference temperature T_0 at which the initial interatomic distance is r_0. When changes are introduced into the material by, for example, material anomaly (*e.g.*, dislocation, permanent slip band, void, micro-cracks), an increase in the order of r_0 in the interatomic distance is triggered, and the increase is denoted as $r_{anomaly}$ in what follows. With $r_{anomaly}$ taken into account, the total interatomic distance $r_{tot}\left(T\right)$, as a consequence of the change in material properties, is rewritten as

$$r_{tot}\left(T\right)=r_0+\alpha\left(T-T_0\right)+r_{anomaly}. \tag{3}$$

With Eqs. (1) and (3), the interatomic force ($F=-{\partial E_{L-J}}/{\partial r}$), linked to T and $r_{anomaly}$, is yielded analytically.

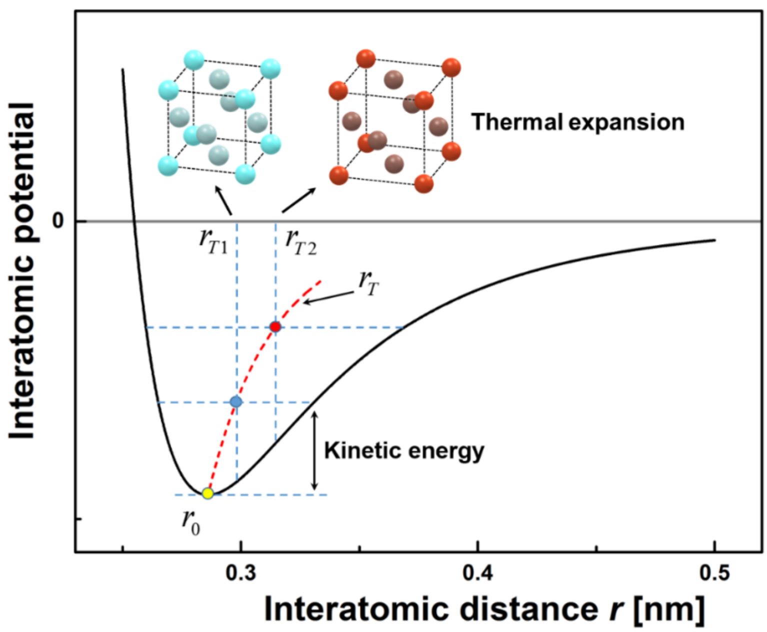

Fig. 1. Interatomic potential $E_{L\text{-}J}(r)$ as a function of the interatomic distance r: the left and right insets in main diagram schematically show the crystal lattice of material at temperature *T1* and *T2*, respectively (r_{T1} and r_{T2}: the average interatomic separation at temperature *T1* and *T2*, respectively, which indicate the increase in average interatomic separation with temperature elevation due to the "an-harmonicity" of interatomic potential).

Now, when a probing elastic wave is emitted into the material, its propagation can be depicted using an equilibrium principle. Without loss of generality, we first consider a one-dimensional scenario [14]. Assuming a disturbance in the deformation of the system of particles, the motion of the n^{th} particle can be depicted using the Newton's second law, which reads

$$
\begin{aligned}
m\frac{d^2u_1^n}{dt^2} &= F_{n,n+1}-F_{n,n-1} \\
&= \left[\frac{\partial E_{L\text{-}J}}{\partial r}+\frac{\partial^2 E_{L\text{-}J}}{\partial r^2}\left(u_1^{n+1}-u_1^n\right)+\frac{1}{2}\frac{\partial^3 E_{L\text{-}J}}{\partial r^3}\left(u_1^{n+1}-u_1^n\right)^2\right]- \\
&\quad \left[\frac{\partial E_{L\text{-}J}}{\partial r}+\frac{\partial^2 E_{L\text{-}J}}{\partial r^2}\left(u_1^{n}-u_1^{n-1}\right)+\frac{1}{2}\frac{\partial^3 E_{L\text{-}J}}{\partial r^3}\left(u_1^{n}-u_1^{n-1}\right)^2\right].
\end{aligned}
\tag{4}
$$

After mathematical manipulations, Eq.(4) can be rewritten as

$$
\begin{aligned}
m\frac{d^2u_1^n}{dt^2} &= \left[\frac{\partial^2 E_{L\text{-}J}}{\partial r^2}\left(\left(u_1^{n+1}-u_1^n\right)-\left(u_1^n-u_1^{n-1}\right)\right)+\frac{1}{2}\frac{\partial^3 E_{L\text{-}J}}{\partial r^3}\left(\left(u_1^{n+1}-u_1^n\right)^2-\left(u_1^n-u_1^{n-1}\right)^2\right)\right] \\
&= \frac{\partial^2 E_{L\text{-}J}}{\partial r^2}r\left(\left(\frac{\partial u_1}{\partial x_1}\right)_{x_1}-\left(\frac{\partial u_1}{\partial x_1}\right)_{x_1-r}\right)+\frac{1}{2}\frac{\partial^3 E_{L\text{-}J}}{\partial r^3}r^2\left(\left(\frac{\partial u_1}{\partial x_1}\right)_{x_1}^2-\left(\frac{\partial u_1}{\partial x_1}\right)_{x_1-r}^2\right).
\end{aligned}
\tag{5}
$$

Dividing Eq.(5) by r, one can get

$$
\frac{m}{r}\frac{d^2u_1}{dt^2}=\frac{\partial^2 E_{L\text{-}J}}{\partial r^2}r\frac{\partial^2 u_1}{\partial x_1^2}+\frac{\partial^3 E_{L\text{-}J}}{\partial r^3}r^2\frac{\partial u_1}{\partial x_1}\frac{\partial^2 u_1}{\partial x_1^2}.
\tag{6}
$$

Letting $\frac{m}{r}=\rho$, Eq.(6) can be reformed as

$$
\begin{gathered}
\frac{\partial^2 u_1}{\partial t^2}=\left(V_p\right)^2[1-\gamma(\frac{\partial u_1}{\partial x_1})]\frac{\partial^2 u_1}{\partial x_1^2}, \\
V_p=\sqrt{\frac{C\left(T,r_{anomaly}\right)r_{anomaly}}{\rho}},\ \gamma=-\frac{D\left(T,r_{anomaly}\right)r_{anomaly}}{C\left(T,r_{anomaly}\right)},
\end{gathered}
\tag{7}
$$

where u_1 signifies the atomic displacement in the wave propagation direction x_1, V_p the wave propagation velocity, ρ the material density, and t the time. γ is a nonlinear parameter. $C\left(T,r_{anomaly}\right)=\partial^2 E_{L-J}/\partial r^2$ and $D\left(T,r_{anomaly}\right)=\partial^3 E_{L-J}/\partial r^3$ are obtained from the differentiations of $E_{L\text{-}J}\left(r\right)$ with regard to r. The above derivation reveals that the variation of the interatomic distance induced by material anomaly can affect the interaction between adjacent particles and the elastic modulus of the material, as a result of which both the wave propagation velocity (reflecting the propagation velocity of disturbance in the atomic displacement) and nonlinear parameters in the governing equation of particulate motion are altered. It is also noteworthy that the material nonlinearity is essentially linked to the features of material at an atomic scale (*i.e.* interatomic distance), and the damage, which is observed at a micro-scale, is a collective and holistic manifestation of the changes in the material at an atomic scale.

Recalling the perturbation method [14], the solution to Eq. (7) can be ascertained, yielding a wave-field that embraces the linear portion u_1^1 and the nonlinear portion u_1^2 ($u_1^2 = u_1^1$). A relative acoustic nonlinearity parameter, $\beta'\left(T, r_{anomaly}\right)$, is defined, serving as a quantitative measure of a nonlinear attribute of elastic wave (*i.e.* second harmonic generation) which reads

$$\beta'\left(T, r_{anomaly}\right) = \frac{A_2\left(T, r_{anomaly}\right)}{A_1\left(T, r_{anomaly}\right)^2} = -\frac{D\left(T, r_{anomaly}\right)}{C\left(T, r_{anomaly}\right)^2} \times K \tag{8}$$

In the above, A_1 and A_2, correlated to T and $r_{anomaly}$, are the amplitudes of u_1^1 and u_1^2, respectively. K is related with the incident frequency and the propagation distance. Considering that the present investigation is focused on the thermal susceptibility of nonlinear wave features, the incident frequency and propagation distance are invariable, as a result of which K signifies a constant. With Eq. (8), the relation between $\beta'\left(T, r_{anomaly}\right)$ and the temperature has been obtained analytically and explicitly, from which the trend of $\beta'\left(T, r_{anomaly}\right)$ against the interatomic distance r is predicted, as shown in **Fig. 2**(a). In **Fig. 2**(a), $r_{anomaly}^1$ and $r_{anomaly}^2$ signify the increase in interatomic distance induced by the two defects of different degrees of severity.

As already stated, measurement of $\beta'\left(T, r_{anomaly}\right)$ is susceptible to contamination from various sources of nonlinearity. Instead of quantifying the absolute value of $\beta'\left(T, r_{anomaly}\right)$

itself, the extent to which $\beta'\left(T, r_{anomaly}\right)$ fluctuates against the ambient temperature variation – namely *thermal susceptibility* – is interrogated. To this end, a thermal susceptibility index (TSI) is defined as

$$TSI = \frac{\Delta\beta'\left(T, r_{anomaly}\right)}{\Delta T}, \tag{9}$$

where $\Delta\beta'\left(T, r_{anomaly}\right)$ denotes the fluctuation in $\beta'\left(T, r_{anomaly}\right)$ when the material is subject to a temperature variation ΔT. With Eq. (9), the relation between the defined *TSI* and the interatomic distance r can be obtained, as shown in **Fig. 2**(b). Analogous to $\beta'\left(T, r_{anomaly}\right)$, TSI is also linked to material properties, and consequently its change can be used inversely to characterize material properties. It is apparent that, at given temperature elevation, material with an anomaly exhibits a higher gradient of $\beta'\left(T, r_{anomaly}\right)$ than its intact counterpart, consequently leading to a higher TSI, see **Fig. 2**(b). *TSI* increases drastically along with the augment in the interatomic distance induced by defect. Therefore, the variation of nonlinear wave features is significant when defects induce increase in interatomic distance and also when the waveguide is subjected to notable temperature elevation. Calibrating the gradient of $\beta'\left(T, r_{anomaly}\right)$ with respect to ambient temperature (via thermal sensitivity), rather than acquiring the $\beta'\left(T, r_{anomaly}\right)$ itself, TSI is immune to interference from various contaminants that might downgrade the measurement precision of the absolute value of $\beta'\left(T, r_{anomaly}\right)$.

The thermal susceptibility of nonlinear attributes of elastic waves, usually considered pessimistically as a detrimental factor in the practical measurement of material acoustic nonlinearity, can now be exploited positively to improve the precision of nonlinear elastic wave-based material characterization, hence enhancing the accuracy and robustness of anomaly imaging under the effect of varying ambient factors.

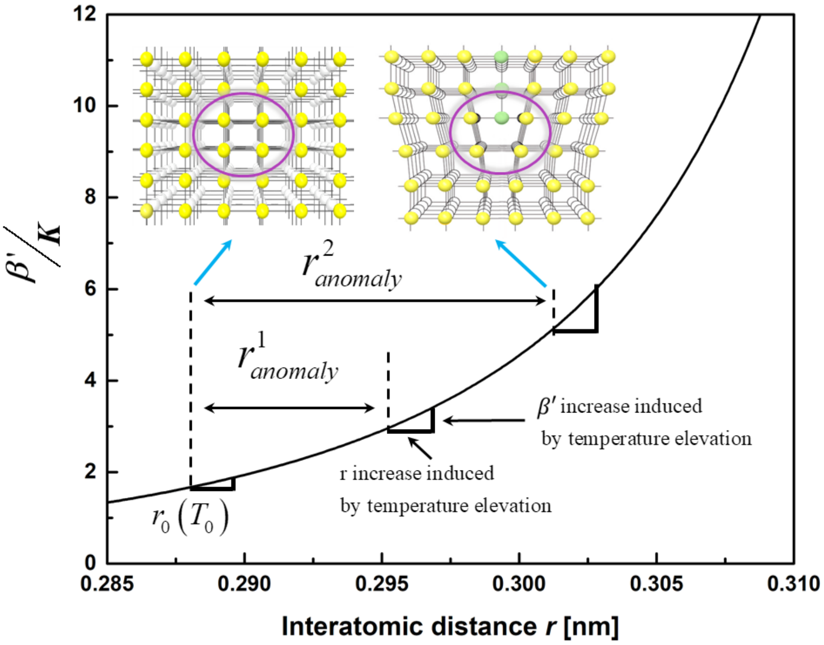

(a)

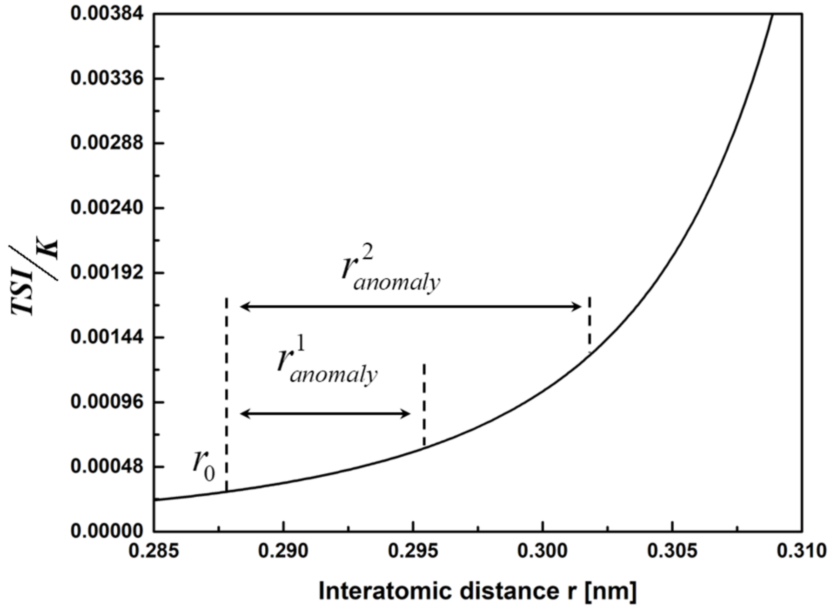

(b)

Fig. 2. (a) Correlation between β'/K and r (insets in main diagram: crystal lattice of material without (left) and with (right) dislocation-type defect): $r^1_{anomaly}$ and $r^2_{anomaly}$ represent increase in interatomic distance induced by material anomalies; (b) correlation

between TSI/K and r for a unit temperature elevation (material with an anomaly exhibiting a higher TSI/K than its intact counterpart).

3. Experimental validation and an application paradigm

3.1. Validation via imaging of fatigue crack

For proof-of-concept validation, an aluminum (Al 6061) waveguide measuring 2mm in thickness is fatigued to the point of suffering a slight degree of material deterioration. Precise imaging of embryonic fatigue damage or fatigue-damage-induced initial material degradation, whose significance cannot be over-emphasized, has been the object of intense effort yet with high challenge [17, 35-37]. Upon completion of the fatigue test, diverse types of defect are generated, including dislocations, permanent slip bands and micro-cracks. These defects jointly lead to an increase in the interatomic distance and intensify the material nonlinearity, leading to the second harmonic generation. To image the fatigue-induced material deterioration in the waveguide, the second harmonic generation – a typical nonlinear feature of elastic waves, is evaluated. For comparison, wave imaging for the fatigue damage is implemented, respectively in a temperature-consistent condition and a temperature-varying condition.

To better comprehend the microstructure of the invisible material deterioration, X-ray radiation diffraction (XRD) testing is performed for the aluminum waveguide before and after the fatigue process, with results presented in **Fig. 3**, from which the diffraction angles and interatomic spacing can be ascertained. Compared with the pristine status of the waveguide, an increase in the *full width at half maximum* (FWHM) of the XRD peak is clearly observed in the fatigued specimen, indicating intensified dislocations and micro-cracks in the waveguide, both of which increase the interatomic distance of the lattice in the fatigued material. This observation authenticates the assertion in section 2 that anomaly in material enlarges interatomic distance therein.

A sensor network consisting of 44 miniaturized lead zirconate titanate (PZT) discs is surface-mounted on the specimen with a distance of 1cm between two adjacent discs, schematically depicted in **Fig. 4**, to enclose an inspection region. This sensor network provides multiple actuating-sensing paths in virtue of the dual-piezoelectricity of PZT, including the two examples Path I and Path II shown in **Fig. 4**. The inspection region is evenly heated with a heat flux of 360℃ for one minute, ensuring uniform temperature elevation throughout the region. Subsequently, the specimen is naturally cooled to the room temperature of 20°C. Note that the process of heating and cooling is completed in a short period in the absence of external loading, and therefore the microstructures of the specimen are invariant during such as heating processing, and no more variations in the specimen (dislocations, PSB, interatomic distances, etc.) are generated. At intervals of a minute in this process of heating and cooling, a ten-cycle Hanning-windowed sinusoidal toneburst at a central frequency of 300 kHz is produced with a nonlinear ultrasonic testing system (RITEC®, RAM-5000 SNAP), to drive each PZT disc in turn and emit a probing elastic wave into the sample. At the selected excitation frequency and the current thickness of the sample, the fundamental symmetric Lamb mode (S_0) dominates the exited probing waves. The phase velocity and group velocity of excited fundamental S_0 mode and corresponding second harmonic mode (S_0) are quasi-matching, and thus in a certain propagation distance, accumulation of second harmonic mode (S_0) is warranted along wave propagation path, as theoretically and experimentally proven elsewhere [14, 38]. Via the dispersion length, this distance for the material used in this study is predicted to be 0.3 m approximately, which is much greater than the distance from any actuator to a sensor in the sensor network. When a PZT disc serves as wave actuator, the other discs in the network are used to acquire wave signals from which nonlinear wave features (i.e. second harmonic modes) are extracted. To mitigate measurement uncertainty, 256 wave signals that are captured under the identical measurement conditions are averaged.

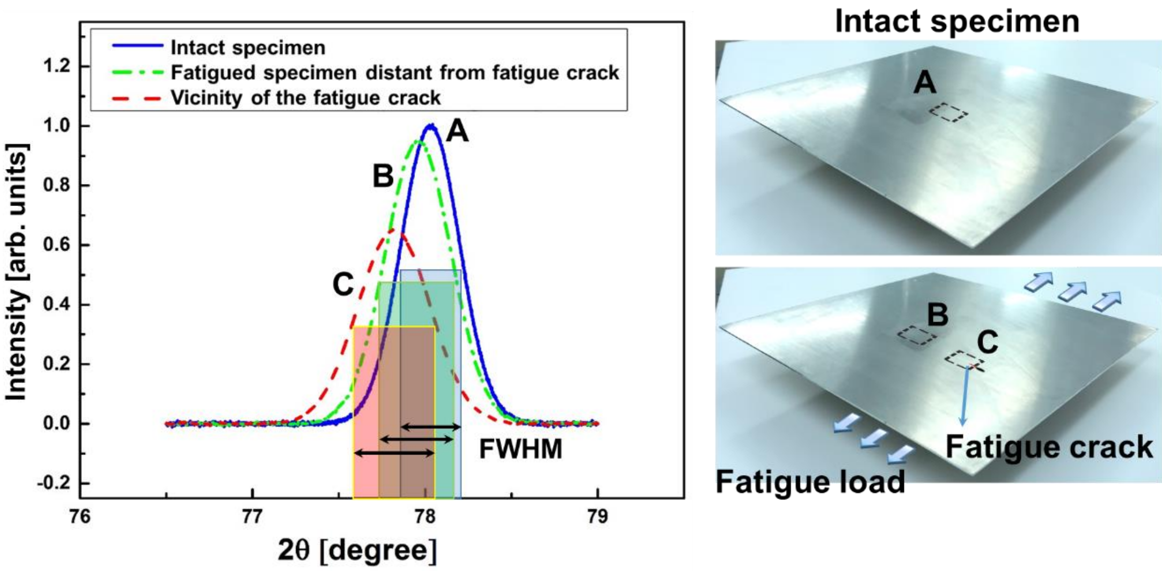

Fig. 3. (311) diffracted peaks in XRD patterns of intact and fatigued specimens: compared with the intact waveguide (region A), an increase in the full width at half maximum (FWHM) of the XRD peak is clearly observed in the fatigued specimen (region B representing material in the fatigued specimen distant from the fatigue crack, and C material in the vicinity of the fatigue crack).

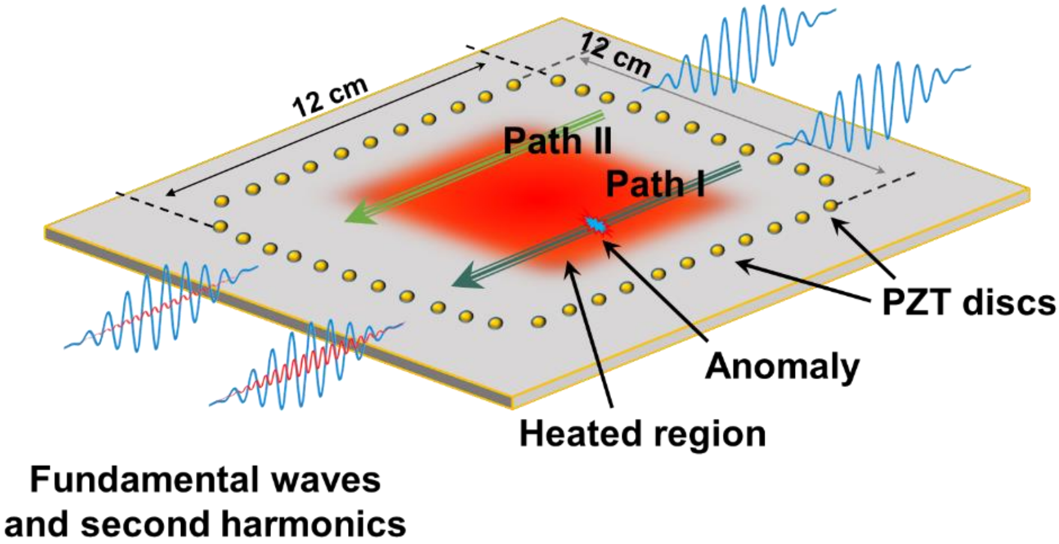

Fig. 4. Experiment set-up: on an Aluminium plate (thickness 2mm), a sensor network consisting of 44 miniaturized lead zirconate titanate (PZT) discs (1cm apart for adjacent discs) is surface-mounted to enclose an inspection region; the inspection region is evenly heated with a heat flux of 360°C for one minute, and naturally cooled to the room temperature of 20°C; a ten-cycle Hanning-windowed sinusoidal toneburst (central frequency 300 kHz) is used to drive each PZT disc in turn and the other discs are used to acquire wave signals from which nonlinear wave features are extracted.

Representative signals acquired via Path I are shown in **Fig. 5**(a), from which the magnitudes of the fundamental and second harmonic modes are extracted and displayed in **Fig. 5**(b). From the velocity of the acquired wave modes, it can be concluded that the first arrival wave packet is the S_0 mode, as highlighted by the rectangle in **Fig. 5**(a). As the propagation distance in the configured sensor network is much smaller than the accumulative distance as analyzed in the above, accumulative second harmonic mode is warranted. On this basis, β' from each path and its variation can be obtained. Note that the defect in the waveguide under investigation is of small scale (e.g., fatigue crack), and under the conditions depicted in this investigation the second harmonics generated by the defect mainly propagate along the propagation direction of incident waves, as proven elsewhere [39], inducing negligible interference of waves along different propagation paths. Thus the probing waves can be modulated by the defect along those propagation paths that traverse the damaged zone, in which generation of second harmonic modes are remarkably induced.

Fig. 5(c) compares the variation of β', respectively obtained via Path II before the fatigue test (blue, corresponding to region A in **Fig. 3**), Path II in the fatigued specimen distant from the fatigue crack (black, corresponding to region B), and Path I in the fatigued specimen traversing the fatigue crack (red, corresponding to region C). **Fig. 5**(c) supports the argument that:

(i) the amplitude of β' increases during the heating process and reverts to its original level after the cooling process;

(ii) fatigue damage – a typical material anomaly – triggers a remarkable augmentation of the amplitude of the β' when compared with its counterpart induced by material nonlinearity in its pristine status; and

(iii) the more severe the fatigue damage, the greater the increase in amplitude.

As the measurement systems and conditions remain unchanged and the microstructures of the specimen are invariant during the heating and cooling process, the changes in nonlinear wave features can be solely attributed to thermal variation. These observations corroborate well the theoretically interpreted temperature-dependence of nonlinear features of elastic waves in section 2. Note that the amplitude of β' reverts to its original level after the cooling process, and this validates the earlier assertion that the heating and cooling processing which is finished in a short period does not lead to changes in the microstructure of the specimen.

Diverse elastic wave imaging methods, as typified by nonlinear phased array imaging [35] and path-based imaging [40], can be recalled to visualize the material anomaly. **Fig. 6**(a) displays the pixelated anomaly image for the fatigued specimen by synthesizing elastic wave signals from all actuating-sensing paths in a sensor network using the path-based imaging algorithm. In the image, the likelihood of the existence of fatigue damage in the waveguide is calculated using *TSI*, with the highest likelihood highlighted that pinpoints the fatigue damage.

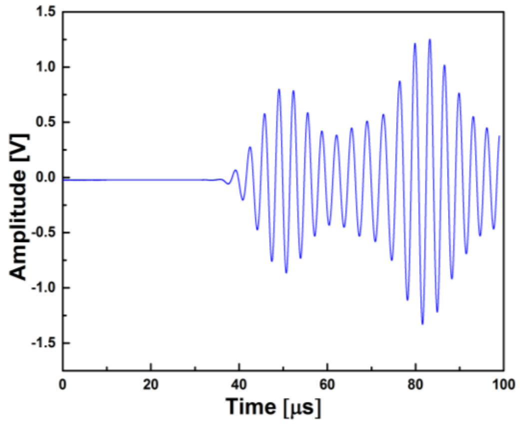

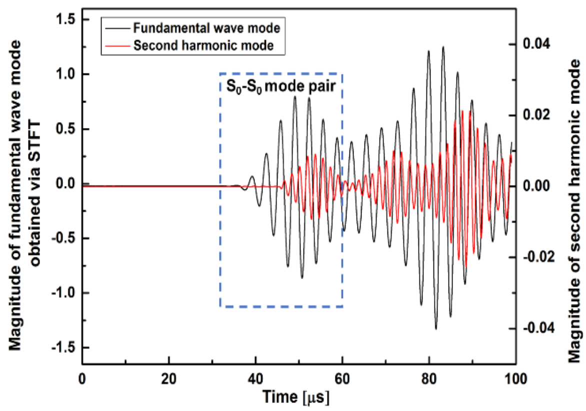

(a) (b)

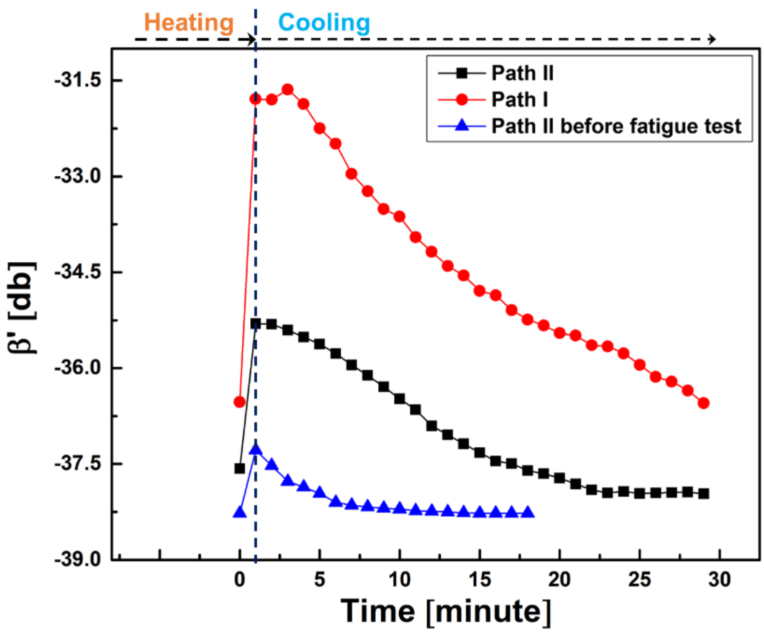

(c)

Fig. 5. (a) Wave signals acquired via Path I; (b) separated wave signals via short time Fourier transform (STFT) processing from which the magnitudes of the fundamental mode (S_0) and second harmonic mode (S_0) can be extracted; and (c) variation of β' from representative paths against time, demonstrating that the paths traversing material with defect manifest higher variations when subjected to temperature elevation.

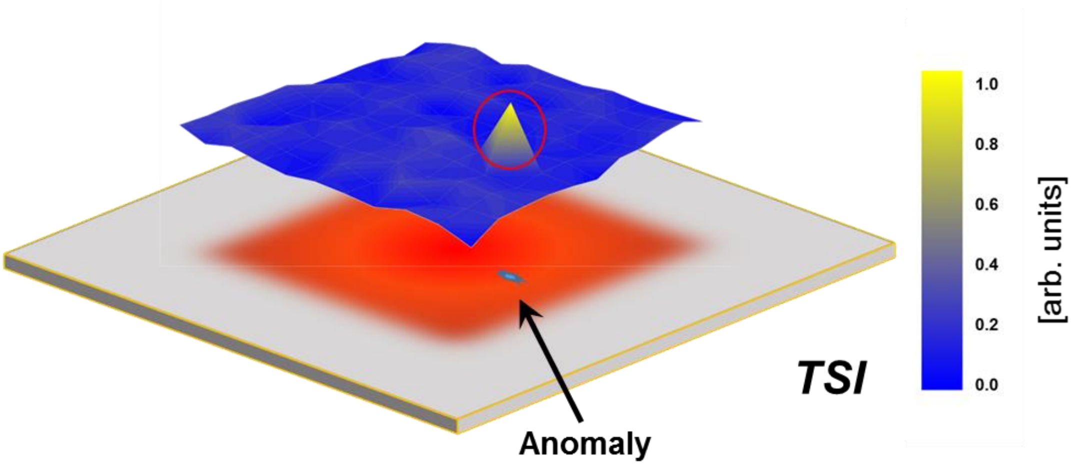

(a)

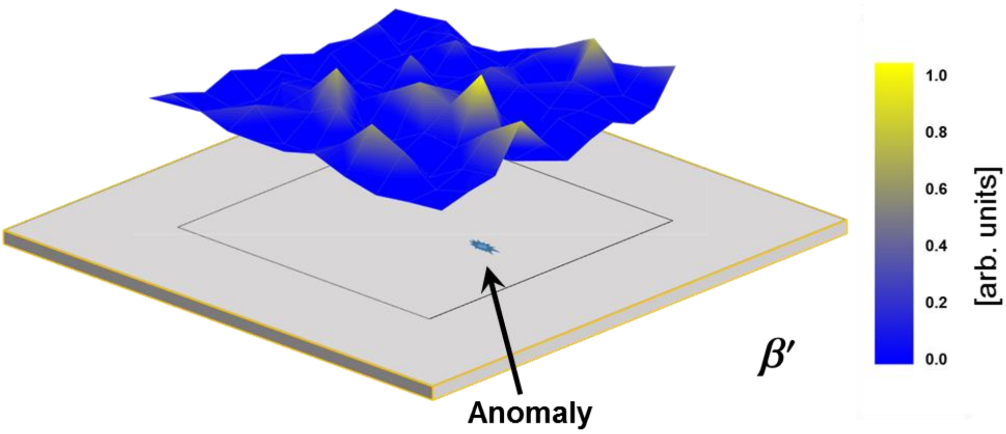

(b)

Fig. 6. Elastic wave imaging results via path-based method using (a) *TSI*, showing high

precision; and (b) absolute value of $\beta'(T, r_{anomaly})$, showing that the fatigued zone in the specimen is not imaged clearly and pseudo spots of fatigue damage are generated.

For comparison, **Fig. 6**(b) displays the image obtained using the absolute value of $\beta'\left(T, r_{anomaly}\right)$ measured at room temperature without a heating and cooling process, in which the fatigued zone in the specimen is not imaged clearly. This is because that besides the nonlinearity induced by the defects in the damaged zone (dislocations, permanent slip bands, and micro-cracks), the second harmonic modes produced by other sources are also introduced in the process of wave generation and acquisition. Typically, those second harmonic modes are generated simultaneously when exciting probing waves using different actuators. Thus, the fatigue damage-induced intensification in $\beta'\left(T, r_{anomaly}\right)$, usually weak in magnitude, is likely overwhelmed by the second harmonic modes linked to other sources. As a result, pseudo spots are observed in the imaging results, as shown in **Fig. 6**(b). In contrast, the imaging approach using *TSI* is of high precision, even when nonlinearity in probing waves generated by diverse sources interferes with the measurement of damage-related nonlinear features. Such a merit of this new imaging approach using *TSI* enhances the accuracy and reliability of anomaly imaging under the interference of ambient noise. It is worth noting that during the cooling process, the cooling rate for the inspected region of the sample is uniform, but the decreasing rate for the defined *TSI* is different along different paths, as shown in **Fig. 5**(c). This phenomenon can be attributed to the fact that along different wave propagation paths, the microstructure features (including dislocations, permanent slip bands and micro-cracks) induced by the fatigue loading are different, as analyzed in the above. When the sample is subject to the ambient temperature variation, the status of these microstructure features can be changed, such as the alternation of contact status of micro-cracks in damaged zone. The reversion of these microstructure features is different from that of the material in the intact region, and thus this induces the extended period for the nonlinear features of waves traversing the damaged zone to return to their original level during the cooling stage.

3.2. Application to imaging of pitting damage

To further examine its applicability and adaptability, the wave imaging approach based on *TSI* is practiced to characterize another particular genre of material degradation – pitting damage. From pitting corrosion in maritime structures through electrical pitting in bearings to debris cloud-induced pitting craters in spacecraft, pitting damage is a typical modality of material degradation and structural lesion in engineering assets subjected to harsh environments. Characterization of this category of defect is of both scientific and practical importance, but is highly challenging and daunting because of its specific manifestation: in most circumstances a pitting damage area features hundreds of small craters and cracks disorderedly clustered over a wide area. **Fig. 7**(a) shows pitting damage generated by a debris cloud in a hyper-velocity impact (HVI) event. Evaluation of pitting damage is a difficult task to fulfill using conventional ultrasonic waves-based approaches with either linear or nonlinear wave features – that is because the sophistication of the pitting damage disturbs probing waves to a high degree of complexity. This complexity applies to all methods using nonlinear attributes of elastic waves, due to the interference from diverse measurement contaminations and also the fact that changes in nonlinear attributes linked to material degradation are obfuscated by the changes due to multiple wave scattering by individual craters and cracks in the pitted area.

XRD tests and scanning electronic microscopy (SEM) analysis are first performed to canvass microstructural characterization of the pitting damage, with results in **Figs.** 7 and 8. It is observed in **Fig.** 7(b) and (c) that the grain boundaries increase dramatically. These grain boundaries represent 2-D defects in the crystal lattice structure in which point defects (e.g., dislocations and voids) are concentrated [41-43]. The XRD diffraction patterns, **Fig. 8**(a), indicate that the dislocation densities increase remarkably in the vicinity of pitting damage. Results from both XRD tests and SEM analysis show that the interatomic distances in the crystal lattice of the material are enlarged, leading to intensification of the thermal susceptibility of $\beta'\left(T, r_{anomaly}\right)$, namely *TSI*, as analyzed in section 2. By calibrating the defined *TSI*, the pitting damage is imaged using the path-based imaging algorithm, in **Fig. 8**(b). Good coincidence is observed with the actual location of the pitting damage, as indicated in **Fig. 7**(a), demonstrating the capability of the proposed method to gauge this type of damage with high sophistication.

Note that to depict the thermal susceptibility of nonlinear wave features accurately, the interatomic potential model must be selected prudently for different materials, leading to different modalities of Eq. (1). In some circumstances, thermal variation may induce changes in nonlinear wave features via a physical mechanism unlike that interpreted in this study, so that the trend of nonlinear wave features to vary thermally might manifest differently. For example, in a metal-matrix composite, elevation of the ambient temperature can result in relaxation of the residual stress in the matrix [28], thereby reducing distortion of the matrix and leading to a decrease in measured acoustic nonlinearity.

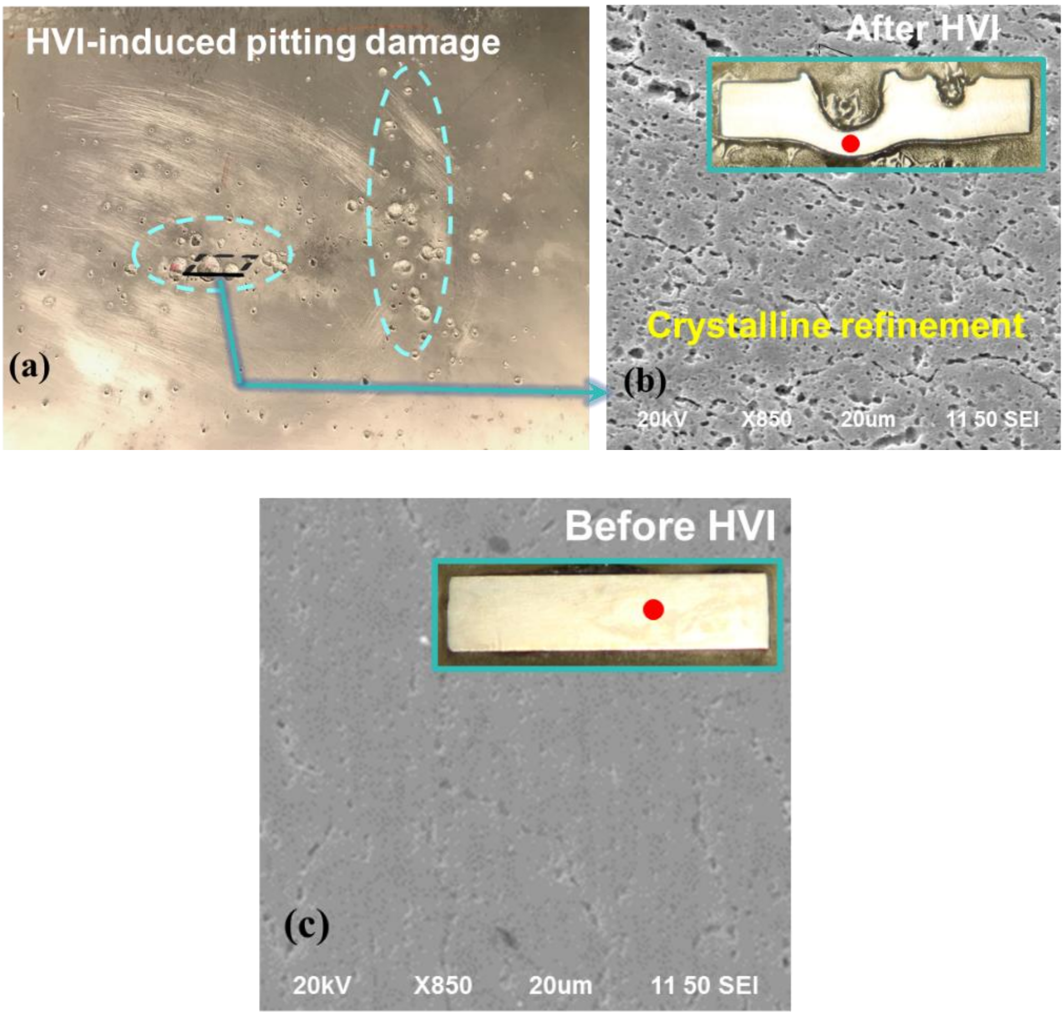

Fig. 7. (a) An aluminum plate waveguide (thickness 3mm) bearing HVI-induced pitting damage; SEM analysis results of the plate (b) after and (c) before HVI: after the HVI, the grain boundaries that represent 2-D defects in the crystal lattice structure increase dramatically, showing obvious enlargement in interatomic distances in the crystal lattice of the material.

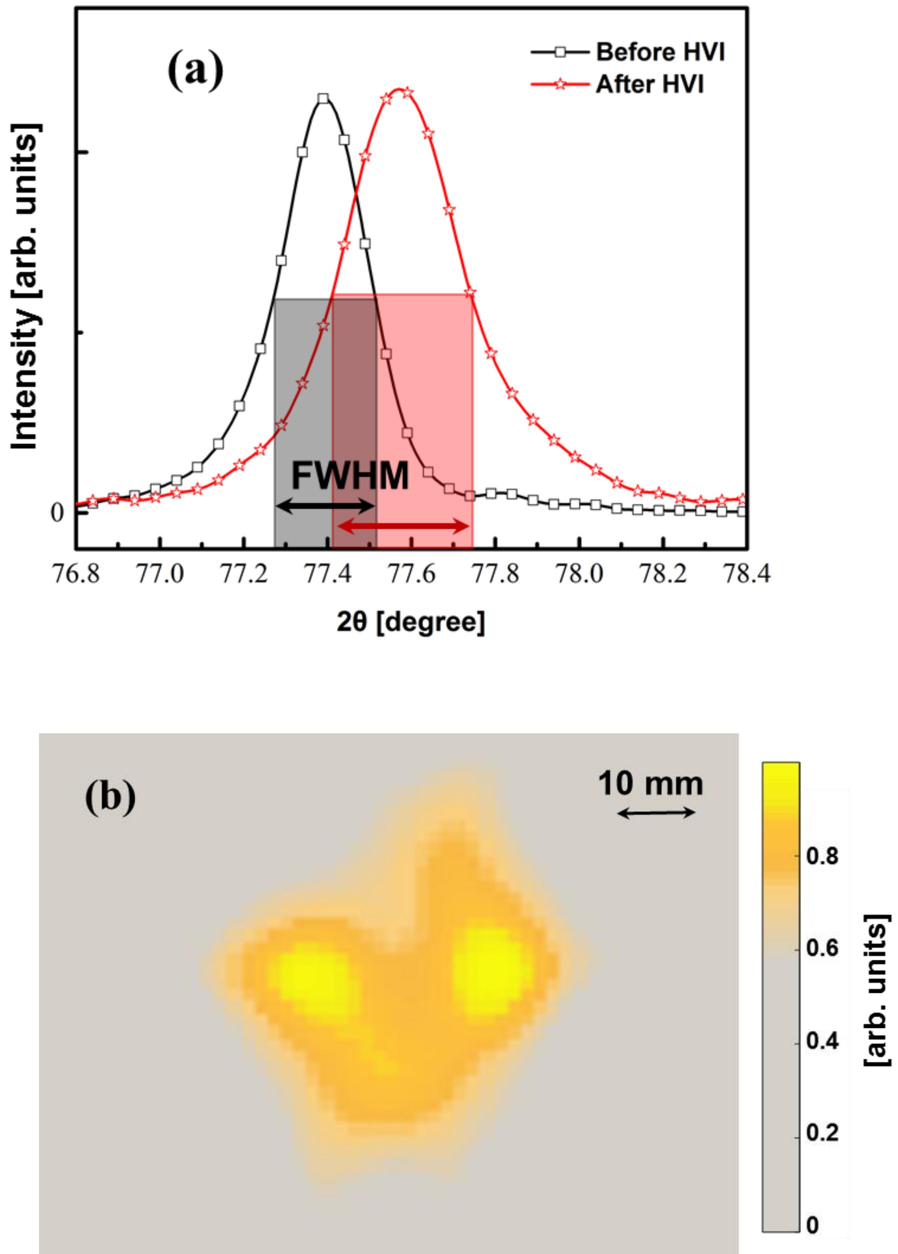

Fig. 8. (a) XRD test results of the waveguide: an increase in the full width at half maximum (FWHM) of the XRD peak is clearly observed in the vicinity of pitting damage fatigued specimen; and (b) elastic wave imaging result using *TSI*, showing good coincidence with the actual location of the pitting damage.

4. Conclusions

Targeting improving the precision and accuracy of material characterization and detection of small-scale defect, we develop a new approach that makes use of the thermal susceptibility of nonlinear attributes of elastic waves, rather than eliminating or compensating for it, to evaluate material acoustic nonlinearity and visualize material anomalies. This approach is physically underpinned by the fact that the material anomaly can impose significant effect on the thermal susceptibility of nonlinear attributes of elastic waves. Experimental results have demonstrated the feasibility of using the thermal susceptibility of acoustic nonlinearity to advance elastic wave-based material anomaly imaging, with improved imaging precision and enhanced accuracy in practical applications. Implementation of the approach can be facilitated either by active temperature control or by passive temperature variation caused by ambient conditions. With these merits, the proposed approach can be applied to the evaluation of diverse material defects including dislocations, vacancies, slag inclusions, and impurities.

Acknowledgments

The work was supported by a General Project (No. 51875492) and a Key Project (No. 51635008) received from the National Natural Science Foundation of China. The authors acknowledge the support from the Hong Kong Research Grants Council via General Research Funds (Nos.: 15201416 and 15212417).

References

[1] Y.-Z. Wang, F.-M. Li, and Y.-S. Wang, "Influences of active control on elastic wave propagation in a weakly nonlinear phononic crystal with a monoatomic lattice chain," *International Journal of Mechanical Sciences,* vol. 106, pp. 357-362, 2016.

[2] K. H. Matlack, H. A. Bradley, S. Thiele, J.-Y. Kim, J. J. Wall, H. J. Jung*, et al.*, "Nonlinear ultrasonic characterization of precipitation in 17-4PH stainless steel," *NDT & E International,* vol. 71, pp. 8-15, 2015.

[3] A. J. Croxford, P. D. Wilcox, B. W. Drinkwater, and P. B. Nagy, "The use of non-collinear mixing for nonlinear ultrasonic detection of plasticity and fatigue," *The Journal of the Acoustical Society of America,* vol. 126, pp. EL117-EL122, 2009.

[4]K. Wang, Y. Li, Z. Su, R. Guan, Y. Lu, and S. Yuan, "Nonlinear aspects of "breathing" crack-disturbed plate waves: 3-D analytical modeling with experimental validation," *International Journal of Mechanical Sciences,* vol. 159, pp. 140-150, 2019.

[5] K. Wang, M. Liu, Z. Su, S. Yuan, and Z. Fan, "Analytical insight into "breathing" crack-induced acoustic nonlinearity with an application to quantitative evaluation of contact cracks," *Ultrasonics,* vol. 88, pp. 157-167, 2018.

[6] P. Liu, H. Sohn, T. Kundu, and S. Yang, "Noncontact detection of fatigue cracks by laser nonlinear wave modulation spectroscopy (LNWMS)," *NDT & E International,* vol. 66, pp. 106-116, 2014.

[7] R. E. Apfel and E. C. Everbach, "Application of the acoustic nonlinearity parameter to tissue composition prediction," *The Journal of the Acoustical Society of America,* vol. 84, pp. S138-S138, 1988.

[8] D. Zhang and X.-F. Gong, "Experimental investigation of the acoustic nonlinearity parameter tomography for excised pathological biological tissues," *Ultrasound in medicine & biology,* vol. 25, pp. 593-599, 1999.

[9] E. Filonenko and V. Khokhlova, "Effect of acoustic nonlinearity on heating of biological tissue by high-intensity focused ultrasound," *Acoustical Physics,* vol. 47, pp. 468-475, 2001.

[10] Y. Liu, K. A. Wear, and G. R. Harris, "Variation of High-Intensity Therapeutic Ultrasound (HITU) Pressure Field Characterization: Effects of Hydrophone Choice, Nonlinearity, Spatial Averaging and Complex Deconvolution," *Ultrasound in Medicine and Biology,* vol. 43, pp. 2329-2342, 2017.

[11] Y. Ohara, T. Mihara, R. Sasaki, T. Ogata, S. Yamamoto, Y. Kishimoto*, et al.*, "Imaging of closed cracks using nonlinear response of elastic waves at subharmonic frequency," *Applied Physics Letters,* vol. 90, p. 011902, 2007.

[12] T. Ju, J. D. Achenbach, L. J. Jacobs, and J. Qu, "Nondestructive evaluation of thermal aging of adhesive joints by using a nonlinear wave mixing technique," *NDT & E International,* vol. 103, pp. 62-67, 2019.

[13] M. Deng, "Cumulative second-harmonic generation of Lamb-mode propagation in a solid plate," *Journal of applied physics,* vol. 85, pp. 3051-3058, 1999.

[14] W. De Lima and M. Hamilton, "Finite-amplitude waves in isotropic elastic plates," *Journal of sound and vibration,* vol. 265, pp. 819-839, 2003.

[15] J. H. Cantrell and W. T. Yost, "Nonlinear ultrasonic characterization of fatigue microstructures," *International Journal of fatigue,* vol. 23, pp. 487-490, 2001.

[16] Y. Xiang, M. Deng, F.-Z. Xuan, and C.-J. Liu, "Effect of precipitate-dislocation interactions on generation of nonlinear Lamb waves in creep-damaged metallic alloys," *Journal of Applied Physics,* vol. 111, p. 104905, 2012.

[17] J.-Y. Kim, L. J. Jacobs, J. Qu, and J. W. Littles, "Experimental characterization of

fatigue damage in a nickel-base superalloy using nonlinear ultrasonic waves," *The Journal of the Acoustical Society of America,* vol. 120, pp. 1266-1273, 2006.
[18] H. Sohn, H. J. Lim, M. P. DeSimio, K. Brown, and M. Derriso, "Nonlinear ultrasonic wave modulation for online fatigue crack detection," *Journal of Sound and Vibration,* vol. 333, pp. 1473-1484, 2014.
[19] S. Liu, A. J. Croxford, S. A. Neild, and Z. Zhou, "Effects of experimental variables on the nonlinear harmonic generation technique," *IEEE transactions on ultrasonics, ferroelectrics, and frequency control,* vol. 58, pp. 1442-1451, 2011.
[20] S. Roy, K. Lonkar, V. Janapati, and F.-K. Chang, "A novel physics-based temperature compensation model for structural health monitoring using ultrasonic guided waves," *Structural Health Monitoring,* vol. 13, pp. 321-342, 2014.
[21] P. B. Dao and W. J. Staszewski, "Cointegration approach for temperature effect compensation in Lamb-wave-based damage detection," *Smart Materials and Structures,* vol. 22, p. 095002, 2013.
[22] C. Nucera and F. Lanza di Scalea, "Nondestructive measurement of neutral temperature in continuous welded rails by nonlinear ultrasonic guided waves," *The Journal of the Acoustical Society of America,* vol. 136, pp. 2561-2574, 2014.
[23] Y. Zhang, V. Tournat, O. Abraham, O. Durand, S. Letourneur, A. L. Duff*, et al.*, "Nonlinear mixing of ultrasonic coda waves with lower frequency-swept pump waves for a global detection of defects in multiple scattering media," *Journal of Applied Physics,* vol. 113, p. 064905, 2013.
[24] O. I. Lobkis and R. L. Weaver, "Coda-wave interferometry in finite solids: recovery of P-to-S conversion rates in an elastodynamic billiard," *Physical review letters,* vol. 90, pp. 254302-254302, 2003.
[25] S. Haupert, G. Renaud, J. Rivière, M. Talmant, P. A. Johnson, and P. Laugier, "High-accuracy acoustic detection of nonclassical component of material nonlinearity," *The Journal of the Acoustical Society of America,* vol. 130, pp. 2654-2661, 2011.
[26] H. J. Lim, H. Sohn, M. P. Desimio, and K. Brown, "Reference-free fatigue crack detection using nonlinear ultrasonic modulation under various temperature and loading conditions," *Mechanical Systems and Signal Processing,* vol. 45, pp. 468-478, 2014.
[27] E. Meeks and R. Arnold, "Temperature Dependence of the Third-Order Elastic Constants of SrTi O 3," *Physical Review B,* vol. 1, p. 982, 1970.
[28] H. Mohrbacher and K. Salama, "The Temperature Dependence of Third-Order Elastic Constants in Metal-Matrix Composites," in *Review of Progress in Quantitative Nondestructive Evaluation*, ed: Springer, 1993, pp. 2091-2097.
[29] C. Nucera and F. L. di Scalea, "Nonlinear wave propagation in constrained solids subjected to thermal loads," *Journal of Sound and Vibration,* vol. 333, pp. 541-554, 2014.
[30] R. Johnson, "Relationship between two-body interatomic potentials in a lattice model and elastic constants. II," *Physical Review B,* vol. 9, p. 1304, 1974.
[31] S. Chaplot, W. Reichardt, L. Pintschovius, and N. Pyka, "Common interatomic potential model for the lattice dynamics of several cuprates," *Physical Review B,* vol. 52, p. 7230, 1995.
[32] A. Pedone, G. Malavasi, M. C. Menziani, A. N. Cormack, and U. Segre, "A new self-consistent empirical interatomic potential model for oxides, silicates, and silica-based glasses," *The Journal of Physical Chemistry B,* vol. 110, pp. 11780-11795, 2006.
[33] P. Gehlen, *Interatomic potentials and simulation of lattice defects*: Springer Science & Business Media, 2012.

[34] C. Kittel, P. McEuen, and P. McEuen, *Introduction to solid state physics* vol. 8: Wiley New York, 1976.
[35] J. Potter, A. Croxford, and P. Wilcox, "Nonlinear ultrasonic phased array imaging," *Physical review letters,* vol. 113, p. 144301, 2014.
[36] R. Lin and T. Ng, "Applications of higher-order frequency response functions to the detection and damage assessment of general structural systems with breathing cracks," *International Journal of Mechanical Sciences,* vol. 148, pp. 652-666, 2018.
[37] A. Reid, M. Marshall, S. Kabra, T. Minniti, W. Kockelmann, T. Connolley*, et al.*, "Application of neutron imaging to detect and quantify fatigue cracking," *International Journal of Mechanical Sciences,* vol. 159, pp. 182-194, 2019.
[38] P. Zuo, Y. Zhou, and Z. Fan, "Numerical and experimental investigation of nonlinear ultrasonic Lamb waves at low frequency," *Appl. Phys. Lett.,* vol. 109, 2016.
[39] G. Tang, L. J. Jacobs, and J. Qu, "Scattering of time-harmonic elastic waves by an elastic inclusion with quadratic nonlinearity," *The Journal of the Acoustical Society of America,* vol. 131, pp. 2570-2578, 2012.
[40] Q. Wang, M. Hong, and Z. Su, "An in-situ structural health diagnosis technique and its realization via a modularized system," *IEEE Transactions on Instrumentation and Measurement,* vol. 64, pp. 873-887, 2015.
[41] L. Priester, *Grain boundaries: from theory to engineering* vol. 172: Springer Science & Business Media, 2012.
[42] M. César, D. Liu, D. Gall, and H. Guo, "Calculated resistances of single grain boundaries in copper," *Physical Review Applied,* vol. 2, p. 044007, 2014.
[43] L. Priester, *Grain boundaries and crystalline plasticity*: John Wiley & Sons, 2013.